ACS APPLIED MATERIALS & INTERFACES

Research Article

www.acsami.org

Synergistic Effects of Binary-Solvent Annealing for Efficient Polymer–Fullerene Bulk Heterojunction Solar Cells

Fu-Chiao Wu,[†] Yi-Hao Li,[†] Chieh-Jen Tsou,[†] Kuo-Cheng Tung,[†] Chia-Te Yen,[†] Fang-Sheng Chou,[†] Fu-Ching Tang,[‡] Wei-Yang Chou,[†] Jrjeng Ruan,[§] and Horng-Long Cheng*,[†]

[†]Department of Photonics, Advanced Optoelectronic Technology Center, National Cheng Kung University, Tainan 701, Taiwan
[‡]Department of Physics, National Cheng Kung University, Tainan 701, Taiwan
[§]Department of Materials Science and Engineering, National Cheng Kung University, Tainan 701, Taiwan

Supporting Information

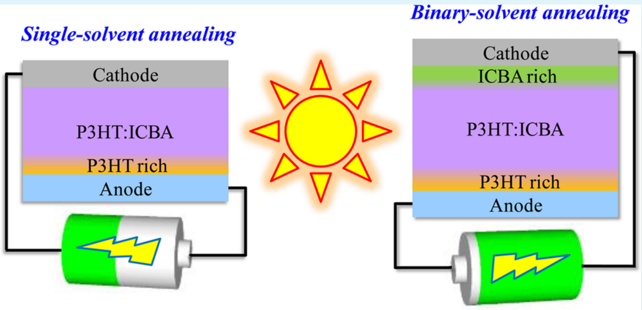

ABSTRACT: Conjugated polymer–fullerene-based bulk-heterojunction (BHJ) organic solar cells (OSCs) have attracted tremendous attention over the past two decades because of their potential to develop low-cost and easy methods to produce energy from light. The complicated microstructure and morphology with randomly organized architecture of these polymer–fullerene-based active layers (ALs) is a key factor that limits photovoltaic performance. In this study, a binary-solvent annealing (BSA) approach was established to improve the poly(3-hexylthiophene):indene-C_{60} bisadduct-based AL for efficient BHJ-type OSCs by varying the second solvents with different boiling points (BP). Thus, we were able to change the evaporation behavior of cosolvents and consequently obtain the various microstructural properties of the AL. An in-depth study was conducted on the solvent-evaporation driven morphology of the active layer under various cosolvent conditions and its effect on the photovoltaic parameters of OSCs. Under the BSA processes, we found that the specimens with low-BP second solvents allows us to observe a more ideal AL for increasing photon absorption and efficient charge transport and collection at the respective electrodes, resulting in enhanced PCE of the corresponding OSCs. By contrast, the specimens with high-BP second solvents exhibit random microstructures, which are detrimental to charge transport and collection and lead to diminished PCE of the corresponding OSCs. By appropriately selecting the composition of a binary solvent, BSA can be employed as an easy method for the effective manipulation of the microstructures of ALs. BSA is a promising technique for the performance enhancement of not only OSCs but also other organic/polymeric-based electronic devices.

KEYWORDS: *organic solar cells, poly(3-hexylthiophene), indene-C_{60} bisadduct, cosolvents, morphology, spectroscopy, atomic force microscopy*

■ INTRODUCTION

In recent years, numerous studies on polymer:fullerene-based organic solar cells (OSCs) have increased the power conversion efficiency (PCE) of OSCs to higher than 10%.[1−3] Given that OSCs are featured by simple and low-cost processes, flexibility, and easy large-scale fabrication, they are considered a promising renewable energy technology. The most widely studied active layer (AL) of an OSC is a composite with bulk heterojunction (BHJ) of an electron donor (D, usually conjugated polymer) and an electron acceptor (A, usually fullerene). In an OSC, the AL absorbs the incident light to generate excitons. Excitons diffuse to the D/A interfaces in the AL to dissociate into holes and electrons. Holes and electrons are then transported to the AL/anode and the AL/cathode interfaces, respectively. Holes are collected by the anode and electrons by the cathode. Finally, an OSC outputs power. The efficient exciton diffusion and dissociation, hole/electron transport, and hole/electron collection at the respective electrodes are necessary for a high-PCE OSC. Exciton dissociation and hole/electron transport are correlated with the microstructural qualities of the AL, and hole/electron collection is relevant to the interfacial qualities of the AL/electrode.[4,5] Therefore, considerable efforts are exerted to improve the microstructures of the AL[6−8] and the interfaces of the AL/electrode[9−11] to enhance the PCE of OSCs.

An ideal morphology of an AL of BHJ-type OSCs has a well-defined D/A interpenetrating network, or a so-called D/A interdigitating structure.[12] In this type of morphology, exciton generation occurs near the D/A interfaces so that excitons are efficiently dissociated into electrons and holes. Then, electrons and holes are transported along continuous pathways to electrodes. Various methods can be used for the morphological amelioration of polymer-based ALs, including thermal anneal-

Received: February 9, 2015
Accepted: August 12, 2015
Published: August 12, 2015

ACS Publications © 2015 American Chemical Society

DOI: 10.1021/acsami.5b05692
ACS Appl. Mater. Interfaces 2015, 7, 18967−18976

ing,[13,14] ternary blend,[15,16] solvent annealing,[17,18] solvent vapor annealing,[19,20] and solvent additive.[21,22] These methods can help the formation of appropriate D/A interpenetrating networks, that is, good D/A contact for efficient exciton dissociation and continuous pathways for efficient charge transport, to improve the photovoltaic (PV) properties of OSCs. Among a variety of methods, solvent-relevant technique is one of the easiest and most effective methods to change the morphologies of polymer-based ALs.[23] The selection of solvents influences the morphologies of polymer-based ALs.[4,24−28] These differences originate from diverse properties of solvents, such as boiling point (BP), solubility of solutes, and vapor pressure. A high-BP solvent used to deposit organic/polymeric materials allows molecules/chains to form ordered structures owing to slow evaporation of the solvent.[4,24,25,27,29] The different solubilities of an organic/polymeric material in different solvents result in various morphologies of thin films.[4,24,28,30] Under low vapor pressure condition, a solvent has slow evaporation rate, resulting in growth of a polymeric thin film that has an ordered structure;[18,31] this process is called solvent annealing. Hence, choosing an appropriate solvent for the fabrication of PSCs is an important issue.

The use of a mixture of different solvents to fabricate OSCs has been observed to enhance the PCE of OSCs compared with a single solvent.[4,24,32−34] This result is attributed to the synergy of properties of different solvents to further improve the morphologies of a polymer-based AL. A solvent additive is doped into a host solvent to induce the evolution of the morphologies of a polymer-based AL into D/A interpenetrating networks during film formation.[4,21,24,33] The addition of a poor solvent into a host solvent can modify the morphologies of an AL by the different solubilities of solutes in the two solvents.[4,24,32,35] In a range of solvent-relevant techniques, a mixed solvent is seldom adopted to perform solvent annealing for the growth of polymer-based ALs. Solvent annealing allows different solvents to have more time to cause synergistic effects on the evolution of the morphologies of a polymer-based AL. Similar to single-solvent annealing, mixed-solvent annealing can also further enhance the PCE of OSCs.

A mixture of two different solvents, called binary solvent, was used in the present study to fabricate a polymer-based AL of a BHJ OSC through binary-solvent annealing (BSA). The polymer-based AL consists of a blend of poly(3-hexylthiophene) (P3HT) as the electron donor with indene-C_{60} bisadduct (ICBA) as the electron acceptor. A high-BP solvent, *o*-dichlorobenzene (DCB; BP, 180 °C), was adopted as the first solvent of the binary solvent. DCB is a commonly used solvent for the growth of P3HT:fullerene-based ALs because of its good solubility for active materials and slow evaporation rate for active materials, thereby facilitating the formation of ordered structures. Two low-BP solvents, namely, chloroform (CF; BP, 61 °C) and dichloromethane (DCM; BP, 38 °C), as well as two high-BP solvents, namely, chlorobenzene (CB; BP, 132 °C) and *o*-xylene (XL, BP: 144 °C), were selected as the second solvents of the binary solvent. The BP of solvents used in this study is summarized in Table S1. Various volume fractions of the second solvents (f_S) were added into DCB to grow a variety of P3HT:ICBA thin films. The specimens were processed by BSA for the same period. In general, high-BP solvents are more suitable than low-BP solvents for solvent annealing. However, unexpected synergistic effects were observed. The P3HT:ICBA solar cells with low-BP solvents as the second solvents (named CF- and DCM-devices) demonstrated an improved PCE, and those from the second solvents with high BP (named CB- and XL-devices) showed a reduced PCE, in comparison with the devices with 0 vol % second solvent (named N-devices). The morphologies and microstructures of diverse P3HT:ICBA thin films were analyzed by spectroscopic methods [absorption spectroscopy, Raman spectroscopy, X-ray diffraction (XRD), and Auger electron spectroscopy], microscopic techniques [atomic force microscopy (AFM), scanning Kelvin probe microscopy (SKPM), and conductive-AFM (c-AFM)], and theoretical calculations. The effects of morphologies of the P3HT:ICBA-based AL on the PV properties of the fabricated BHJ PSCs are discussed.

■ EXPERIMENTAL SECTION

Sample Preparation. P3HT:ICBA-based OSCs were fabricated using indium tin oxide (ITO, 7 Ω/□)-coated glass as substrates. The surface of the ITO was treated by oxygen plasma at 50 W for 3 min. Poly(3,4-ethylenedioxythiophene):poly(styrenesulfonate) (PEDOT:PSS, Clevios P AI 4083) was spin-coated on the ITO and then baked at 150 °C for 30 min to form 33 nm thick hole extraction layers. P3HT (Rieke Metals) and ICBA (Lumtec) in a weight ratio of 1:1 were dissolved in various binary solvents at a concentration of 34 mg/mL to prepare P3HT:ICBA solutions. Different P3HT:ICBA solutions were spin-coated on the PEDOT:PSS at 1400 rpm for 25 s and then placed in small Petri dishes for 1 h for solvent annealing. After solvent annealing, the specimens were baked at 150 °C for 5 min to produce a variety of P3HT:ICBA-based ALs. All preparation procedures of the AL films were conducted in a nitrogen-filled glovebox. Finally, 40 nm calcium and 100 nm aluminum were thermally evaporated sequentially on the P3HT:ICBA to complete the OSCs.

Characterization. The electrical properties of the P3HT:ICBA solar cells were characterized using a LabVIEW-controlled Keithley 2400 SourceMeter. A solar simulator equipped with an AM1.5G filter was adopted as the light source with an intensity of 100 mW/cm^2. The electrical measurement of devices was performed in a nitrogen-filled glovebox. The absorption spectra of P3HT:ICBA thin films were acquired by a GBC Cintra 202 UV/vis spectrometer (resolution <0.9 nm). The Raman spectra of specimens were recorded via a Jobin Yvon LabRAM HR spectrometer with a 532 nm solid-state laser as the excitation source (resolution <0.4 cm^{-1}). The XRD spectra of specimens were obtained using a Rigaku RINT 2000 diffractometer (wavelength of X-ray, 1.5406 Å; step size, 0.01°). AFM, SKPM, and c-AFM were employed (Park System XE-100 AFM) under ambient air condition. Chromium−gold-coated silicon cantilevers (NSC14/CR-AU, Mikromasch) were adopted for SKPM measurements. The probes were calibrated on highly ordered pyrolitic graphite with a work function of 4.65 eV. Platinum−iridium (Pt−Ir) coated silicon cantilevers (PPP-CONTSCPT, Nanosensors) were used for c-AFM measurements. Elementary depth profiles of the P3HT:ICBA AL films were determined using Auger electron spectroscopy (VG Scientific, MICROLAB 350) coupled with argon etching. Primary electron acceleration voltage was 10 keV. Argon ion beam used for sputtering had energy of 3 kV and beam current of approximately 19 μA/cm^2. Energy ranges investigated in this technique were as follows for each element: S LM1 at 152 eV, C KL1 at 271 eV, and O KL1 at 508 eV.

Theoretical Calculations. The reorganization energy (λ_{reorg}) of a polythiophene was computed through the Gaussian 09 program suite. The geometries of a single polythiophene at neutral and cation states were individually optimized using density functional theory (DFT) at B3LYP/6-31G(d) level under periodic boundary conditions. After geometry optimization, the optimized neutral and cation geometries of a single polythiophene were obtained. The single-point energies of a single polythiophene with optimized neutral geometry at neutral and cation states (denoted as E_0^0 and E_0^1, respectively), as well as that with optimized cation geometry at neutral and cation states (denoted as E_1^0 and E_1^1, respectively), were calculated by DFT at B3LYP/6-31G(d) level. The difference between E_0^0 and E_1^0 and that between E_0^1 and E_1^1 resulted in the λ_{reorg} of a single polythiophene.[36,37]

RESULTS AND DISCUSSION

The PV characteristics of various P3HT:ICBA OSCs are summarized in Figure 1. The variations in the PV characteristics of devices from various second solvents are different. For the CF- and DCM-devices, the short circuit current density (J_{SC}) augments with increasing f_S. At f_S of 50 vol %, a J_{SC} of up to 10 mA/cm^2 was produced. The open circuit voltage (V_{OC}) and fill factor (FF) of both the CF- and DCM-devices gradually reduce with increasing f_S. Compared with the N-devices, the CF- and DCM-devices perform an improved PCE. Specifically at f_S of 40−50 vol %, the PCE can exceed 5% because of the significantly augmented J_{SC}. Using the CF single solvent, the corresponding OSCs only show fair PV performance with PCE of ca. 3.2%. The device from neat DCM at the same concentration of solutes cannot be completed due to its poor solubility for P3HT. For the CB- and XL-devices, the J_{SC} and FF are close to those of the N-devices at f_S of 20 vol %. In contrast to the CF- and DCM-devices, the J_{SC} of the CB- and XL-devices remarkably decreases at f_S higher than 20 vol %. The CB- and XL-devices also produce a more significantly reduced FF than the CF- and DCM-devices. The V_{OC} of both the CB- and XL-devices with f_S lower than 40 vol % is close to that of the N-devices. However, with increasing f_S above 40 vol %, the V_{OC} shows a more rapid diminution than that in the CF- and DCM-devices. Therefore, the CB- and XL-devices with f_S of 20 vol % perform a PCE similar to that of the N-devices. At f_S above 20 vol %, the severe reduction in J_{SC}, V_{OC}, and FF results in a much lower PCE of the CB- and XL-devices than the N-devices. The PCE values (below 2.0%) are similar to those of using the single solvent CB and XL (ca. 1.7%). The microstructural features of P3HT:ICBA thin films from different second solvents are analyzed to investigate the origins of the different variations in the electrical characteristics of various devices.

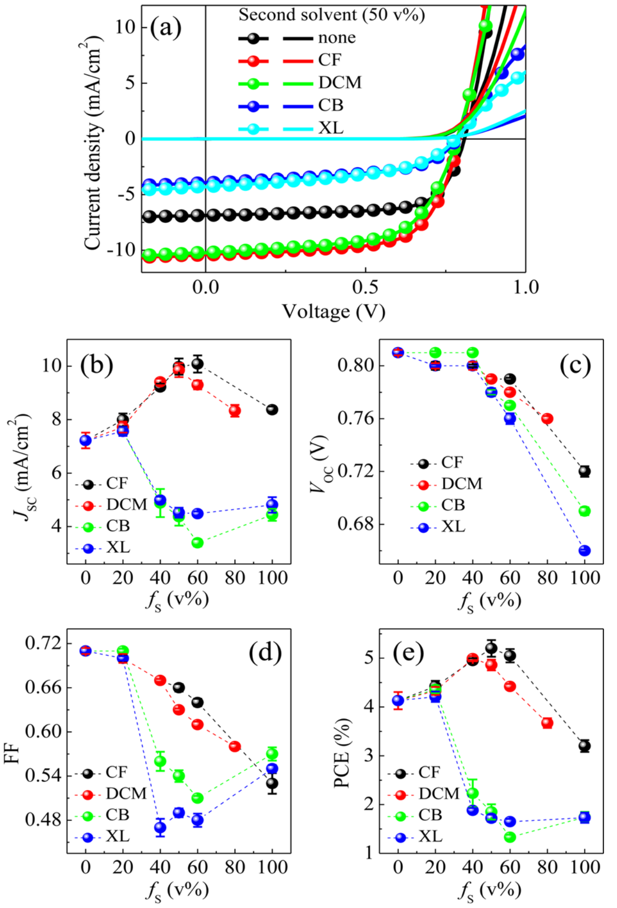

Figure 1. (a) Current−voltage curves of P3HT:ICBA-based OSCs in the light (lines + circles) and in the dark (lines). The AL films were processed with and without 50 vol % second solvents. The extracted PV parameters of the P3HT:ICBA-based OSCs as a function of the volume fraction of the second solvent (f_S) in the BSA process: (b) short-circuit current density (J_{SC}), (c) open-circuit voltage (V_{OC}), (d) fill factor (FF), and (e) power conversion efficiency (PCE).

Figure 2 shows the normalized absorption spectra of P3HT:ICBA thin films from various second solvents. The absorption in the spectra is mainly from P3HT.[36] The absorption measured for energies below approximately 2.3 eV is mainly from the π-stacked aggregate (i.e., crystalline P3HT) and that above approximately 2.3 eV is mainly caused by unaggregated molecules or short oligomers (i.e., amorphous P3HT).[39−41] Following previous methodology based on an H-aggregate model,[39−41] the absorption spectra of the films could be separated into crystalline and amorphous parts (Supporting Information, Figure S1). Thus, the spectra are normalized by the absorbance at 2.3 eV to study the changes in the crystalline and amorphous portions of P3HT. For the P3HT:ICBA thin films from the second solvents of CF or DCM (CF- or DCM-specimens), as shown in Figure 2a,b, the absorbance at approximately 2.80 and 2.07 eV increases with increasing f_S, indicating the increment of the amorphous P3HT and crystalline P3HT, respectively. With regard to the P3HT:ICBA thin films with CB or XL as the second solvents (CB- or XL-specimens), the absorption spectra of the specimens with f_S of 20 vol % are similar to that of the normal specimen (0 vol % second solvent, N-specimen), as shown in Figure 2c,d. As f_S

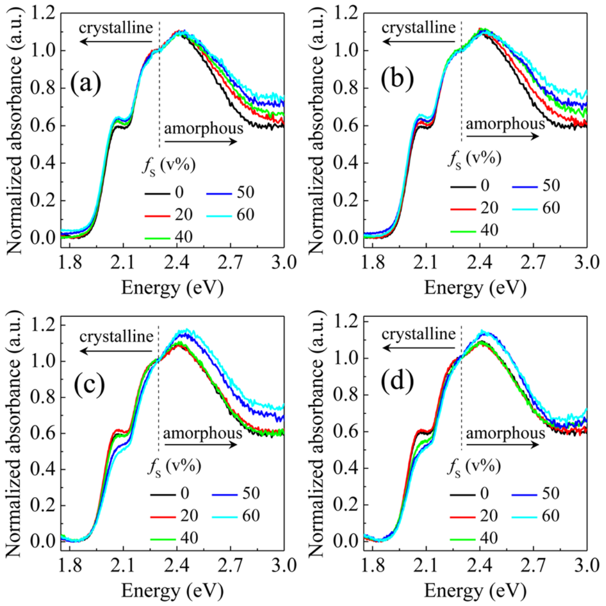

Figure 2. Normalized absorption spectra of P3HT:ICBA thin films with various volume fractions of (a) CF, (b) DCM, (c) CB, and (d) XL as second solvents; f_S is the volume fraction of a second solvent. The dashed line represents the location of 2.3 eV.

increases to 40 vol %, the absorbance of both the CB- and XL-specimens at above 2.3 eV remains unchanged. However, the absorbance at approximately 2.07 eV decreases, especially for the XL-specimen, which is different from the CF- and DCM-specimens. This result indicates a decrease in the crystalline portion of P3HT. With further increase in f_S above 40 vol % (Figure 2c,d), the absorbance at above 2.3 eV rises and that at around 2.07 eV decreases. Thus, these specimens possess an augmented amorphous P3HT and a diminished crystalline P3HT.

The molecular features of P3HT in the crystalline portion can be determined from the absorption spectrum of the crystalline P3HT.[38,39] The absorption from crystalline P3HT in P3HT:ICBA thin films was defined through fitting the absorption spectra of the thin films (Figure 3a), the N-specimen, for example, by the modified Franck−Condon equation:[38,39,41]

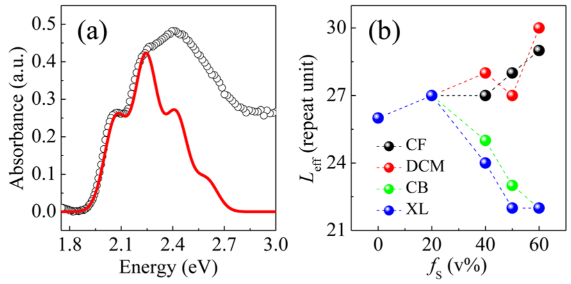

Figure 3. (a) Absorption spectrum (open circles) of the P3HT:ICBA thin film made by a single solvent DCB. The absorption from the crystalline P3HT of the specimen defined by the modified Franck−Condon equation is shown as the red line in panel a. (b) Effective conjugation length (L_{eff}) of the crystalline P3HT in P3HT:ICBA thin films from different second solvents versus the volume fractions of second solvents (f_S).

$$A \propto \sum_{m=0} \left(\frac{e^{-S}S^m}{m!}\right)\left(1 - \frac{W e^{-S}}{2E_P}G_m\right)^2 \Gamma(\hbar\omega - E_{0-0} - mE_P) \tag{1}$$

where A is the relative absorption intensity, m is the vibrational level, S is the Huang−Rhys factor assumed to be 1,[39,41] W is the exciton bandwidth, E_P is the energy of the main vibrational mode of P3HT coupled with the electronic transition, G_m is a constant equal to $\Sigma_{n(\neq m)}S^n/n!(n - m)$ (n is the vibrational quantum number), Γ is a Gaussian function, ω is the vibrational frequency, and E_{0-0} is the energy of the 0−0 electronic transition. After the fitting procedure, the W of each specimen was obtained (Supporting Information for details, Figure S1). With the increase in f_S, the W of the CF- and DCM-specimens decreases, but that of the CB- and XL-specimens increases (Figure S1). The values of interchain excitonic coupling (J) of the crystalline P3HT in various specimens were then calculated from the equality of $W = 4J$ (for free excitons).[38,39] The effective conjugation length (L_{eff}) of the crystalline P3HT in different specimens was estimated[38] on the basis of the relationship between J and L_{eff} of P3HT, $J \sim L_{eff}^{-1.81}$, as shown in Figure 3b. The L_{eff} of the crystalline P3HT extends with rising f_S in both the CF- and DCM-specimens. In the CB- and XL-specimens, the L_{eff} of the crystalline P3HT is close to that of N-specimen at f_S of 20 vol %. At f_S above 20 vol %, the L_{eff} shortens with rising f_S. Considering the results observed in the absorption spectra, the variation trends in the L_{eff} of the crystalline P3HT and in the crystalline portion of P3HT are consistent, that is, increased portion along with extended L_{eff} and decreased portion along with shortened L_{eff}.

The features of molecules in the amorphous region of P3HT in different P3HT:ICBA thin films were studied through Raman spectroscopy. A 532 nm light source was used to excite the amorphous P3HT of the thin films. Figure 4a shows the Raman spectrum of the N-specimen. The peak at around 1448 cm^{-1} (ν_1 band) indicates the vibrational mode of the symmetric C═C stretching deformation in the aromatic thiophene ring of P3HT.[40] The Raman spectra of the other specimens also have the ν_1 band. The ν_1 bands of various specimens are shown in Figure 4b. The ν_1 bands of the CF- and DCM-specimens are similar to that of the N-specimen after the addition of 20 vol % second solvents. At f_S above 20 vol %, an apparent red shift of ν_1 bands was found with increasing f_S, indicating the L_{eff} of the amorphous P3HT becomes longer.[40] The ν_1 bands of the CB- and XL-specimens are similar to that of the N-specimen after the addition of second solvents below 40 vol %. As f_S increases to above 40 vol %, the ν_1 bands show an obvious blue shift, indicating the L_{eff} of the amorphous P3HT is decreased, contrary to the CF- and DCM-specimens.

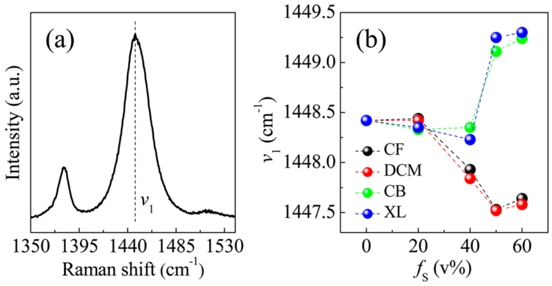

Figure 4. (a) Raman spectrum of the P3HT:ICBA thin film made by a single solvent DCB and excited by a 532 nm laser. The dashed line in panel a indicates the location of the ν_1 band. (b) Locations of the ν_1 band of P3HT:ICBA thin films from different second solvents as a function of the volume fractions of second solvents (f_S).

The surface morphologies of various P3HT:ICBA thin films were examined by AFM. Figure 5 shows the AFM images of different specimens. The phase separation in the N-specimen is obvious but not severe. The domains of the phases are large, complete, and continuous. All the morphologies of the CF- and DCM-specimens with different f_S look similar to that of the N-specimen, as shown in Figures 5a and 5b. In the CB- and XL-specimens with f_S below 40 vol %, their morphologies are also similar to that of the N-specimen (Figure 5c,d). However, as f_S increases to higher than 40 vol %, the CB- and XL-specimens display a different morphology. Figures 5c and 5d show that the phase separation becomes unapparent, and the phases evolve into small, incomplete, and discontinuous domains.

The microstructural features of P3HT:ICBA thin films from different second solvents are summarized, and the corresponding device performance is discussed as follows: The crystalline region of P3HT in the CF- and DCM-specimens increases, in which the L_{eff} of P3HT chains is extended with increasing f_S. The amorphous region of P3HT is also incremental with increasing f_S. Among amorphous P3HT, the L_{eff} of P3HT chains is approximately unchanged at f_S of 20 vol %. At f_S above 20 vol %, the L_{eff} of P3HT chains extends with rising f_S. The crystalline P3HT is correlated with charge transport in a

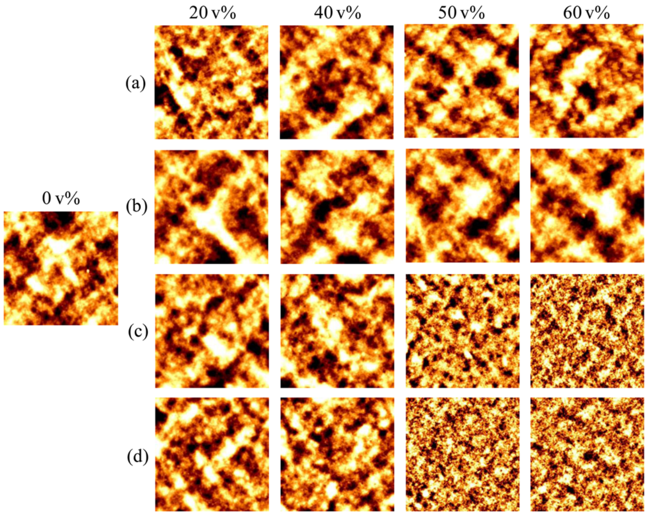

Figure 5. AFM topographies (5 × 5 μm) of P3HT:ICBA thin films made by various volume fractions of (a) CF, (b) DCM, (c) CB, and (d) XL as second solvents.

solar cell device.[38,42] According to Marcus theory, the charge transfer rate between two similar molecules is controlled by two parameters, λ_{reorg} and charge transfer integral.[36,37] On the basis of the DFT calculations in this study, an extension in the L_{eff} of a polythiophene chain results in a reduction of λ_{reorg}, following a relationship of $\lambda_{\mathrm{reorg}} \sim L_{\mathrm{eff}}^{-1}$, as shown in Figure 6a. A smaller λ_{reorg} leads to a higher charge transfer rate.[36,37] Therefore, charge transport in the CF- and DCM-devices is improved, resulting in an enhanced J_{SC}. Charge transfer integral is relevant to the configurations of two molecules.[11,36,37] Figure 6b shows the XRD pattern of the N-specimen. The diffraction peak located at approximately 5.3° (2θ) represents the (100) lattice plane of edge-on P3HT stacking that constructs lamellar supramolecular structures piling up along the *a*-axis (the direction of charge transport in a solar cell device),[43] as shown in the inset of Figure 6b. The XRD patterns of other specimens also show the (100) peaks. As a result, the configuration of two adjacent P3HT molecules along the direction of charge transport in all of the specimens is edge-to-edge type. The edge-to-edge type of a molecular configuration leads to a very small charge transfer integral[11,37] so that the charge transfer rate is dominated by λ_{reorg}. The interaction of the amorphous P3HT with ICBA influences the exciton dissociation and built-in voltage of a solar cell device.[38] A longer L_{eff} of the amorphous P3HT interacting with ICBA leads to a smaller built-in voltage and a more inefficient exciton dissociation,[15,38] resulting in lower V_{OC} and FF for the CF- and DCM-devices.

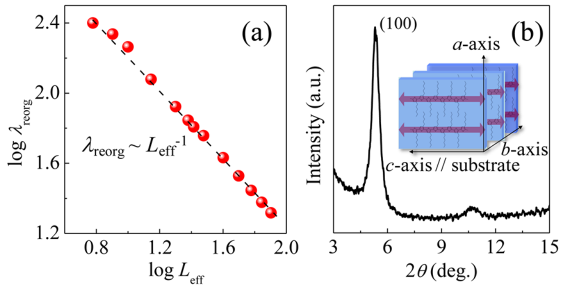

Figure 6. (a) Logarithmic reorganization energy (λ_{reorg}, meV) of a polythiophene chain as a function of logarithmic effective conjugation length (L_{eff}, repeat unit) of a polythiophene chain. The dashed line serves as a guide line. The relationship between λ_{reorg} and L_{eff} is shown in panel a. (b) XRD spectrum of the P3HT:ICBA thin film from 0 vol % second solvent. The inset illustrates the lamellar supramolecular structures formed by stacked edge-on P3HT.

Meanwhile, the crystalline region of P3HT and the L_{eff} of P3HT chains in the CB- and XL-specimens are nearly unchanged as f_{S} is 20 vol %. With increasing f_{S} higher than 20 vol %, the crystalline P3HT and its L_{eff} decrease. At f_{S} lower than 40 vol %, the L_{eff} values of the amorphous P3HT are approximately unchanged. At f_{S} above 40 vol %, the L_{eff} of the amorphous P3HT is decreased. The shortened L_{eff} of the crystalline P3HT results in a low charge transfer rate because of high λ_{reorg}. Hence, the CB- and XL-devices show low J_{SC} and FF. Amorphous P3HT with decreased L_{eff} interacting with ICBA results in a big built-in voltage,[15,38] leading to a high V_{OC} of a solar cell device. However, the CB- and XL-devices produce a reduced V_{OC}.

Figure 7a shows the thicknesses of various P3HT:ICBA thin films. The thickness of the CF- and DCM-specimens increases with increasing f_{S}. The thicknesses of the CB- and XL-specimens are still close to that of the N-specimen with increasing f_{S}. A thicker AL film can absorb more light to generate more excitons. Thus, it may benefit PV performance. Based on the comparison of the PV characteristics of Figure 1 with those of Figure 7a, the OSCs with thickest AL films do not exhibit the optimal PV performance. These excitons dissociate into charges and are then transported to the respective electrodes to contribute to the PV performance. Thus, significantly improved performance of OSCs processed using cosolvent with 40−50 vol % CF and DCM cannot be possibly achieved by thickness effects only. We further examined the series resistance (R_{s}), which is the sum of the contact resistance (R_{c}) and the bulk resistance (R_{b}) of the AL, of different P3HT:ICBA solar cells, as shown in Figure 7b. Lower R_{s} value corresponds to improved R_{c} (i.e., good contact between AL and electrodes) and/or R_{b} (i.e., good charge conduction pathway within the AL to the electrodes). At f_{S} of 20 vol %, the R_{s} values of the four types of devices are similar to that of the N-devices. With increasing f_{S} above 20 vol %, the CF- and DCM-devices (thick specimens) show R_{s} close to that of the N-devices, and the CB- and XL-devices (thin specimens) show a significant increase in R_{s}. This result indicates that the CF- and DCM-devices can produce higher J_{SC} values than the N-devices because of similar R_{s} values along with higher thickness. However, CB- and XL-devices produce lower J_{SC} values because of similar thicknesses along with higher R_{s}.

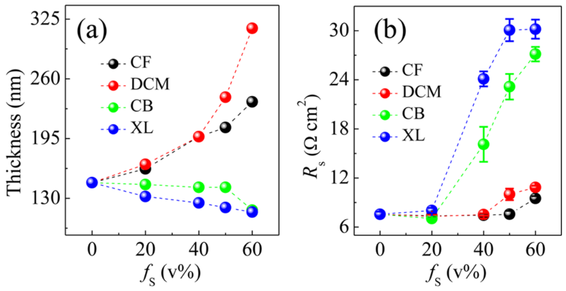

Figure 7. (a) Thicknesses of P3HT:ICBA thin films made by different second solvents versus the volume fraction of second solvents (f_{S}). (b) Series resistance (R_{s}) of P3HT:ICBA solar cells from various second solvents as a function of f_{S}.

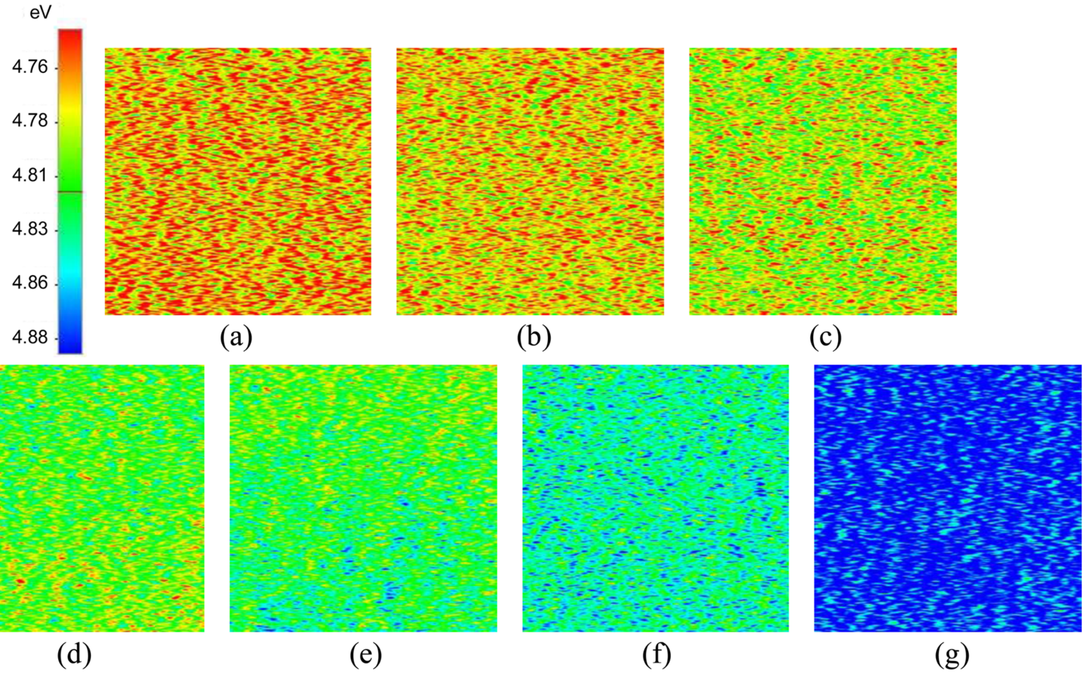

Figure 8. 2D work function images (5 μm × 5 μm) of various films from SKPM measurements: (a) pure P3HT film, (b−f) P3HT:ICBA films, and (g) pure ICBA film. The P3HT:ICBA films were made under different conditions: (b) BSA process with 50 vol % XL, (c) BSA process with 50 vol % XL, (d) using the DCB single solvent, (e) BSA process with 50 vol % DCM, and (f) BSA process with 50 vol % CF.

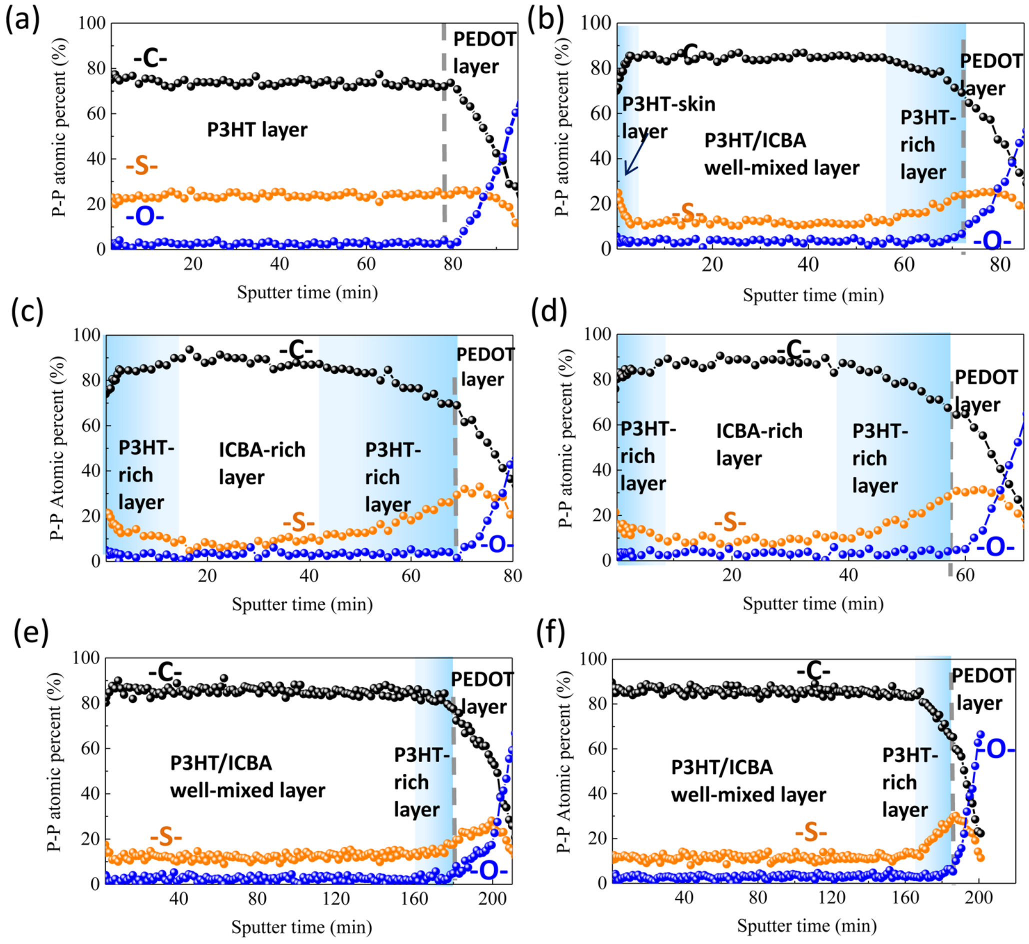

Figure 9. Peak-to-peak depth profiles by Auger electron spectroscopy: (a) pure P3HT film and (b−f) P3HT:ICBA films all upon the PEDOT:PSS layer. The P3HT:ICBA films were made by (b) single solvent DCB and by cosolvents with 50 vol % of (c) CB, (d) XL, (e) DCM, and (f) CF.

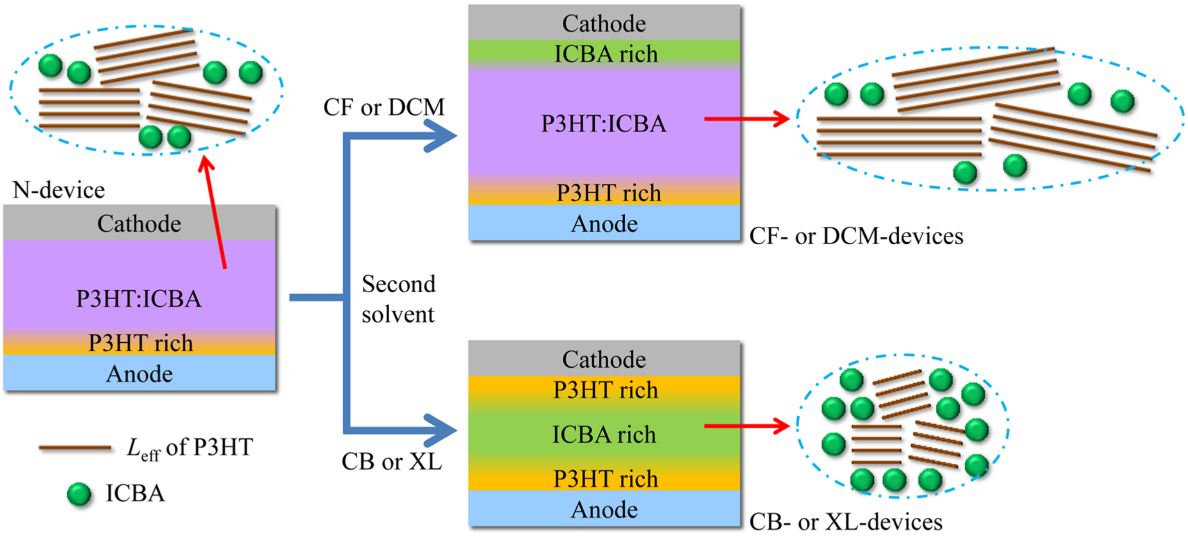

Figure 10. Illustration of the microstructures of different P3HT:ICBA-based OSCs.

The solar cells in this study are conventional configuration of devices. The top surfaces of the P3HT:ICBA AL films are correlated with the electron injection/transport in OSCs. The surface characteristics of various P3HT:ICBA AL films were studied by SKPM as shown in Figure 8. The N-specimen, pure P3HT, and pure ICBA films all made by a single solvent of DCB were also shown for comparison. Compared with the N-specimen (Figure 8d), the surface work function of the CB- and XL-specimens becomes lower (Figure 8b,c) and closer to that of the neat P3HT film (Figure 8a). By contrast, the CF- and DCM-specimens both perform increased work function (Figure 8e,f), and the values are close to that of the neat ICBA film (Figure 8g), especially for the CF-specimen. Compared with the N-specimen, the SKPM results indicate that the CB- and XL-specimens possess a P3HT-enrich top layer and the CF- and DCM-specimens possess an ICBA-enrich top layer. The ICBA is an electron acceptor and favors electron transport, whereas P3HT is an electron donor and favors hole transport. Thus, the formed ICBA-enrich top layer of the CF- and DCM-specimens is more beneficial for electron transport and collection by the cathode, which leads to an augmented J_{SC}. By contrast, the formed P3HT-enriched top layer would impede electron transport and collection by the cathode, which results in inefficient electron extraction of the CB- and XL-devices and thus a decreased J_{SC}. Horizontal geometry of c-AFM measurements was performed to confirm this idea (a detailed description of the experimental setup and results can be found in the Supporting Information, Figure S2). Using a Pt-coated tip with a match of Fermi energy with the highest occupied molecular orbital of P3HT, the neat P3HT film and XL-specimen exhibit a larger hole current compared with the N-specimen. By contrast, the neat ICBA film and CF-specimen showed an almost no-hole current. These results confirm the components of the top layer of these different P3HT:ICBA AL films.

Auger electron spectroscopy was used to investigate the internal structure of the P3HT:ICBA AL films, and the depth profiles of the AL films upon the PEDOT:PSS layer were analyzed by recording the −C− (carbon), −S− (sulfur), and −O− (oxygen) concentrations in combination with ion-beam milling depending on the thickness of the films, as shown in Figure 9. Signals of −S− and −O− can be used to indicate the P3HT distribution along the thickness of AL films and the position of the PEDOT:PSS layer, respectively, because ICBA has no sulfur and oxygen elements and P3HT has no oxygen element. Pure P3HT film shows a uniform −C− and −S− signals through the film. A relatively high −S− signal at the top and bottom layers was observed for the N-specimen, which indicates P3HT-enrich top and bottom layers. At the middle layer, uniform −C− and −S− signals suggest a well-mixed P3HT:ICBA layer. As for CB- and XL-specimens, the curves of −C− and −S− signals exhibit concave−down and concave−up shapes, respectively. This result would suggest P3HT-enrich top and bottom layers, and ICBA-enrich middle layer. Comparing Figure 9 panel c with panels b and d, the CB-specimen has a thicker P3HT-enrich top layer than the XL- and N-specimens. The observation is consistent with the SKPM results that the surface characteristic of the CB specimen is closest to the pure P3HT film, followed by the XL-specimen, and finally the N-specimen. Figure 9e,f shows that the CF- and DCM-specimens have a uniform distribution of P3HT and ICBA across most of the film and a thin P3HT-enrich bottom layer. A slightly relatively high −S− signal can still be observed at the surface of the DCM-specimen. Such a situation could not be found in the CF-specimen. SKPM and c-AFM confirmed the results that the CF-specimen has the largest amount of ICBA on the surface among the specimens. It was followed by the DCM-specimen.

The resulting microstructures of P3HT:ICBA-based films with different second solvents are illustrated in Figure 10. All the specimens exhibit a P3HT-enrich bottom layer. Thus, holes could no doubt be extracted by the PEDOT:PSS/ITO electrode. Among them, the CB- and XL-specimens contain the thickest P3HT-enrich bottom layer. Meanwhile, many P3HT molecules are distributed near the cathode to prevent electrons to the cathode. More ICBA molecules are located in the middle of the films, thereby blocking hole conduction within the films. The reduced region and L_{eff} of the crystalline P3HT are detrimental to hole transport. Thus, the electron/hole pathways become incomplete and discontinuous, thereby increasing the probability of charge recombination. These features lead to the occurrence of inefficient transport of electrons and holes to the cathode and the anode, respectively. Hence, a severe decrease of the J_{SC} and FF of the devices is observed. Although the shortened L_{eff} of the amorphous P3HT (Figure 4b) induces a higher built-in voltage to increase the V_{OC} of the devices, the worse microstructures of the devices result in a decrease in the V_{OC}.[44,45] The reduced J_{SC}, V_{OC}, and FF result in a much lower PCE of the CB- and XL-devices. Compared with the N-devices, more ICBA molecules in the CF- and DCM-devices were located near the cathode, which enhanced the electron transport/extraction from ICBA to the cathode. The region and L_{eff} of the crystalline P3HT are also increased, which leads to improved exciton diffusion (narrow W value benefits exciton diffusion) and hole transport. A homogeneous distribution of P3HT and ICBA across the films (Auger electron spectroscopy analysis) combined with excellent PV feature, a well-mixed P3HT:ICBA middle layer could be highlighted. The thickness of the AL is also augmented. These features allow more electrons and holes to be transported efficiently to the cathode and anode, respectively. Therefore, the devices can produce higher J_{SC}. Although the extension of the L_{eff} of the amorphous P3HT (Figure 4b) causes a smaller built-in voltage and is unfavorable to exciton dissociation, the remarkable increase in J_{SC} improves the PCE of the CF- and DCM-devices by generating decreased V_{OC} and FF of the devices.

In this study, BSA was adopted to fabricate the P3HT:ICBA active layer. High-BP solvents in single-solvent annealing can result in better microstructures of polymer-based ALs because the microstructural features are mainly influenced by solvent—solute interaction. However, the evolution of the microstructures of polymer-based ALs by BSA is more complicated than that by single-solvent annealing. More interactions occur during BSA, including the interactions of first solvent with solute, second solvent with solute, and first solvent with second solvent, thus leading to a multistage solvent evaporation rate (Figure S3). By contrast, single-solvent annealing with DCB solvent results in a nearly constant solvent evaporation rate. When the BSA process using combined DCB and low-BP second solvents was adopted, an appropriate phase-separated morphology of the P3HT:ICBA blending film with higher thickness (Figure 10) was observed not only in enhancing photon absorption but also in improving charge transport to the respective electrodes. During P3HT:fullerene blend films solidification, P3HT crystallinity was mainly influenced by drying time during solvent casting and by the degree of disturbance of fullerene. The fullerene clusters were formed in blend films affected by the solubility of fullerene. Herein, the low-boiling second solvents (i.e., CF and DCM) preferentially dissolve ICBA over P3HT,[46,47] thereby improving the solubility of ICBA in cosolvents. Moreover, incorporating CF and DCM increases the drying time during BSA process, thereby providing the P3HT chains sufficient time to self-organize, which leads to increased L_{eff}. Reducing the solvent evaporation rate is possible if an additional force exists in cosolvent systems.[48] On the contrary, the drying time could not be increased by adding CB and XL in the BSA process, thereby suggesting a normal mix of cosolvents without significant additional force. A faster drying rate of solvent does not facilitate self-organization of P3HT, thereby decreasing L_{eff}, and it does not obtain a proper phase-separated microstructure (Figure 10) for improving the PV performance. Accordingly, a combination of two high-BP solvents is unnecessary to obtain a better microstructure of a P3HT:fullerene-based AL.

■ CONCLUSIONS

The BSA approach was used to fabricate the P3HT:ICBA-based OSCs. A high-BP solvent (first solvent) was mixed with different second solvents, including two low-BP and two high-BP solvents, to obtain a variety of binary solvents. Unlike single-solvent annealing, uncommon synergistic effects from BSA on the microstructures of P3HT:ICBA thin films were observed. The use of low-BP solvents as the second solvents facilitates the development of morphological features that are favorable for photon absorption, exciton diffusion, efficient charge transport, and collection. As a result, the PCE of the devices is enhanced. By contrast, the use of high-BP solvents as the second solvents causes the formation of undesirable microstructural features, leading to inefficient charge transport and collection; hence, a reduced PCE. Compared with single-solvent annealing, the PCE of P3HT:ICBA-based OSCs is successfully improved by BSA. BSA can also be adopted to fabricate ALs of other types of organic/polymeric electronic devices, that is, the microstructural features of ALs can be easily manipulated to generate various functionalities for different types of devices by selecting a proper combination of solvents. Therefore, BSA is a simple and effective technique to optimize the performance of organic/polymeric electronic devices.

■ ASSOCIATED CONTENT

Ⓢ Supporting Information

The Supporting Information is available free of charge on the ACS Publications website at DOI: 10.1021/acsami.5b05692.

> Boiling point of the solvents; supplementary absorption spectra and theoretical fitting procedure; horizontal geometry of c-AFM measurements; solvent evaporation during film casting. (PDF)

■ AUTHOR INFORMATION

Corresponding Author

*E-mail: shlcheng@mail.ncku.edu.tw.

Notes

The authors declare no competing financial interest.

■ ACKNOWLEDGMENTS

This work was supported by the Ministry of Science and Technology, Taiwan, through Grant NSC 101-2221-E-006-163-MY3 and 102-ET-E-006-005-ET. We are grateful to the National Center for High-Performance Computing of Taiwan for computer time and facilities.

■ REFERENCES

(1) Chen, C.-C.; Chang, W.-H.; Yoshimura, K.; Ohya, K.; You, J.; Gao, J.; Hong, Z.; Yang, Y. An Efficient Triple-Junction Polymer Solar Cell Having a Power Conversion Efficiency Exceeding 11%. *Adv. Mater.* **2014**, *26*, 5670−5677.

(2) Liu, Y.; Zhao, J.; Li, Z.; Mu, C.; Ma, W.; Hu, H.; Jiang, K.; Lin, H.; Ade, H.; Yan, H. Aggregation and Morphology Control Enables Multiple Cases of High-Efficiency Polymer Solar Cells. *Nat. Commun.* **2014**, *5*, 5293.

(3) Liao, S.-H.; Jhuo, H.-J.; Yeh, P.-N.; Cheng, Y.-S.; Li, Y.-L.; Lee, Y.-H.; Sharma, S.; Chen, S.-A. Single Junction Inverted Polymer Solar Cell Reaching Power Conversion Efficiency 10.31% by Employing Dual-Doped Zinc Oxide Nano-Film as Cathode Interlayer. *Sci. Rep.* **2014**, *4*, 6813.

(4) Liu, F.; Gu, Y.; Shen, X.; Ferdous, S.; Wang, H.-W.; Russell, T. P. Characterization of the Morphology of Solution-Processed Bulk

Heterojunction Organic Photovoltaics. *Prog. Polym. Sci.* **2013**, *38*, 1990−2052.

(5) Gomez, E. D.; Loo, Y.-L. Engineering the Organic Semiconductor-Electrode Interface in Polymer Solar Cells. *J. Mater. Chem.* **2010**, *20*, 6604−6611.

(6) Nguyen, T. L.; Choi, H.; Ko, S.-J.; Uddin, M. A.; Walker, B.; Yum, S.; Jeong, J.-E.; Yun, M. H.; Shin, T. J.; Hwang, S.; Kim, J. Y.; Woo, H. Y. Semi-Crystalline Photovoltaic Polymers with Efficiency Exceeding 9% in a ∼ 300 nm Thick Conventional Single-Cell Device. *Energy Environ. Sci.* **2014**, *7*, 3040−3051.

(7) Vandewal, K.; Himmelberger, S.; Salleo, A. Structural Factors That Affect the Performance of Organic Bulk Heterojunction Solar Cells. *Macromolecules* **2013**, *46*, 6379−6387.

(8) Huang, Y.; Wen, W.; Mukherjee, S.; Ade, H.; Kramer, E. J.; Bazan, G. C. High-Molecular-Weight Insulating Polymers Can Improve the Performance of Molecular Solar Cells. *Adv. Mater.* **2014**, *26*, 4168−4172.

(9) Yang, T.; Wang, M.; Duan, C.; Hu, X.; Huang, L.; Peng, J.; Huang, F.; Gong, X. Inverted Polymer Solar Cells with 8.4% Efficiency by Conjugated Polyelectrolyte. *Energy Environ. Sci.* **2012**, *5*, 8208−8214.

(10) Khan, T. M.; Zhou, Y.; Dindar, A.; Shim, J. W.; Fuentes-Hernandez, C.; Kippelen, B. Organic Photovoltaic Cells with Stable Top Metal Electrodes Modified with Polyethylenimine. *ACS Appl. Mater. Interfaces* **2014**, *6*, 6202−6207.

(11) Tang, F.-C.; Wu, F.-C.; Yen, C.-T.; Chang, J.; Chou, W.-Y.; Chang, S.-H. G.; Cheng, H.-L. A Nanoscale Study of Charge Extraction in Organic Solar Cells: The Impact of Interfacial Molecular Configurations. *Nanoscale* **2015**, *7*, 104−112.

(12) Günes, S.; Neugebauer, H.; Sariciftci, N. S. Conjugated Polymer-Based Organic Solar Cells. *Chem. Rev.* **2007**, *107*, 1324−1338.

(13) Bergqvist, J.; Lindqvist, C.; Bäcke, O.; Ma, Z.; Tang, Z.; Tress, W.; Gustafsson, S.; Wang, E.; Olsson, E.; Andersson, M. R.; Inganäs, O.; Müller, C. Sub-Glass Transition Annealing Enhances Polymer Solar Cell Performance. *J. Mater. Chem. A* **2014**, *2*, 6146−6152.

(14) Zhao, G.; He, Y.; Li, Y. 6.5% Efficiency of Polymer Solar Cells Based on poly(3-hexylthiophene) and Indene-C_{60} Bisadduct by Device Optimization. *Adv. Mater.* **2010**, *22*, 4355−4358.

(15) Wu, F.-C.; Hsu, S.-W.; Cheng, H.-L.; Chou, W.-Y.; Tang, F.-C. Effects of Soft Insulating Polymer Doping on the Photovoltaic Properties of Polymer-Fullerene Blend Solar Cells. *J. Phys. Chem. C* **2013**, *117*, 8691−8696.

(16) Chi, C.-Y.; Chen, M.-C.; Liaw, D.-J.; Wu, H.-Y.; Huang, Y.-C.; Tai, Y. A Bifunctional Copolymer Additive to Utilize Photoenergy Transfer and to Improve Hole Mobility for Organic Ternary Bulk-Heterojunction Solar Cell. *ACS Appl. Mater. Interfaces* **2014**, *6*, 12119−12125.

(17) Li, G.; Shrotriya, V.; Huang, J.; Yao, Y.; Moriarty, T.; Emery, K.; Yang, Y. High-Efficiency Solution Processable Polymer Photovoltaic Cells by Self-Organization of Polymer Blends. *Nat. Mater.* **2005**, *4*, 864−868.

(18) Li, G.; Yao, Y.; Yang, H.; Shrotriya, V.; Yang, G.; Yang, Y. Solvent Annealing" Effect in Polymer Solar Cells Based on Poly(3-hexylthiophene) and Methanofullerenes. *Adv. Funct. Mater.* **2007**, *17*, 1636−1644.

(19) Bull, T. A.; Pingree, L. S. C.; Jenekhe, S. A.; Ginger, D. S.; Luscombe, C. K. The Role of Mesoscopic PCBM Crystallites in Solvent Vapor Annealed Copolymer Solar Cells. *ACS Nano* **2009**, *3*, 627−636.

(20) Chen, H.; Hsiao, Y.-C.; Hu, B.; Dadmun, M. Control of Morphology and Function of Low Band Gap Polymer−Bis-Fullerene Mixed Heterojunctions in Organic Photovoltaics with Selective Solvent Vapor Annealing. *J. Mater. Chem. A* **2014**, *2*, 9883−9890.

(21) Lai, Y.-Y.; Liao, M.-H.; Chen, Y.-T.; Cao, F.-Y.; Hsu, C.-S.; Cheng, Y.-J. Compact Bis-Adduct Fullerenes and Additive-Assisted Morphological Optimization for Efficient Organic Photovoltaics. *ACS Appl. Mater. Interfaces* **2014**, *6*, 20102−20109.

(22) Liu, C.-M.; Su, Y.-W.; Jiang, J.-M.; Chen, H.-C.; Lin, S.-W.; Su, C.-J.; Jeng, U.-S.; Wei, K.-H. Complementary Solvent Additives Tune the Orientation of Polymer Lamellae, Reduce the Sizes of Aggregated Fullerene Domains, and Enhance the Performance of Bulk Heterojunction Solar Cells. *J. Mater. Chem. A* **2014**, *2*, 20760−20769.

(23) Chen, L. M.; Hong, Z. R.; Li, G.; Yang, Y. Recent Progress in Polymer Solar Cells: Manipulation of Polymer: Fullerene Morphology and the Formation of Efficient Inverted Polymer Solar Cells. *Adv. Mater.* **2009**, *21*, 1434−1449.

(24) Etxebarria, I.; Ajuria, J.; Pacios, R. Solution-Processable Polymeric Solar Cells: A Review on Materials, Strategies and Cell Architectures to Overcome 10%. *Org. Electron.* **2015**, *19*, 34−60.

(25) Müller-Buschbaum, P. The Active Layer Morphology of Organic Solar Cells Probed with Grazing Incidence Scattering Techniques. *Adv. Mater.* **2014**, *26*, 7692−7709.

(26) Ruderer, M. A.; Guo, S.; Meier, R.; Chiang, H.-Y.; Körstgens, V.; Wiedersich, J.; Perlich, J.; Roth, S. V.; Müller-Buschbaum, P. Solvent-Induced Morphology in Polymer-Based Systems for Organic Photovoltaics. *Adv. Funct. Mater.* **2011**, *21*, 3382−3391.

(27) Dang, M. T.; Wantz, G.; Bejbouji, H.; Urien, M.; Dautel, O. J.; Vignau, L.; Hirsch, L. Polymeric Solar Cells Based on P3HT:PCBM: Role of the Casting Solvent. *Sol. Energy Mater. Sol. Cells* **2011**, *95*, 3408−3418.

(28) Chueh, C.-C.; Yao, K.; Yip, H.-L.; Chang, C.-Y.; Xu, Y.-X.; Chen, K.-S.; Li, C.-Z.; Liu, P.; Huang, F.; Chen, Y.; Chen, W.-C.; Jen, A. K.-Y. Non-Halogenated Solvents for Environmentally Friendly Processing of High-Performance Bulk-Heterojunction Polymer Solar Cells. *Energy Environ. Sci.* **2013**, *6*, 3241−3248.

(29) Chang, J.-F.; Sun, B.; Breiby, D. W.; Nielsen, M. M.; Sölling, T. I.; Giles, M.; McCulloch, I.; Sirringhaus, H. Enhanced Mobility of Poly(3-hexylthiophene) Transistors by Spin-Coating from High-Boiling-Point Solvents. *Chem. Mater.* **2004**, *16*, 4772−4776.

(30) Graham, K. R.; Wieruszewski, P. M.; Stalder, R.; Hartel, M. J.; Mei, J.; So, F.; Reynolds, J. R. Improved Performance of Molecular Bulk-Heterojunction Photovoltaic Cells through Predictable Selection of Solvent Additives. *Adv. Funct. Mater.* **2012**, *22*, 4801−4813.

(31) Yang, H.; Shin, T. J.; Yang, L.; Cho, K.; Ryu, C. Y.; Bao, Z. Effect of Mesoscale Crystalline Structure on the Field-Effect Mobility of Regioregular Poly(3-hexyl thiophene) in Thin-Film Transistors. *Adv. Funct. Mater.* **2005**, *15*, 671−676.

(32) Sun, S.; Salim, T.; Wong, L. H.; Foo, Y. L.; Boey, F.; Lam, Y. M. A New Insight into Controlling Poly(3-hexylthiophene) Nanofiber Growth through a Mixed-Solvent Approach for Organic Photovoltaics Applications. *J. Mater. Chem.* **2011**, *21*, 377−386.

(33) Guo, X.; Zhou, N.; Lou, S. J.; Smith, J.; Tice, D. B.; Hennek, J. W.; Ortiz, R. P.; Navarrete, J. T. L.; Li, S.; Strzalka, J.; Chen, L. X.; Chang, R. P. H.; Facchetti, A.; Marks, T. J. Polymer Solar Cells with Enhanced Fill Factors. *Nat. Photonics* **2013**, *7*, 825−833.

(34) Lin, S.-H.; Lan, S.; Sun, J.-Y.; Lin, C.-F. Influence of Mixed Solvent on the Morphology of the P3HT:Indene-C60 Bisadduct (ICBA) Blend Film and the Performance of Inverted Polymer Solar Cells. *Org. Electron.* **2013**, *14*, 26−31.

(35) Kim, J.-H.; Park, J. H.; Lee, J. H.; Kim, J. S.; Sim, M.; Shim, C.; Cho, K. Bulk Heterojunction Solar Cells Based on Preformed Polythiophene Nanowires via Solubility-Induced Crystallization. *J. Mater. Chem.* **2010**, *20*, 7398−7405.

(36) Brédas, J.-L.; Beljonne, D.; Coropceanu, V.; Cornil, J. Charge-Transfer and Energy-Transfer Processes in π-Conjugated Oligomers and Polymers: A Molecular Picture. *Chem. Rev.* **2004**, *104*, 4971−5003.

(37) Coropceanu, V.; Cornil, J.; Filho, D. A.; da, S.; Olivier, Y.; Silbey, R.; Brédas, J.-L. Charge Transport in Organic Semiconductors. *Chem. Rev.* **2007**, *107*, 926−952.

(38) Wu, F.-C.; Huang, Y.-C.; Cheng, H.-L.; Chou, W.-Y.; Tang, F.-C. Importance of Disordered Polymer Segments to Microstructure-Dependent Photovoltaic Properties of Polymer-Fullerene Bulk-Heterojunction Solar Cells. *J. Phys. Chem. C* **2011**, *115*, 15057−15066.

(39) Clark, J.; Silva, C.; Friend, R. H.; Spano, F. C. Role of Intermolecular Coupling in the Photophysics of Disordered Organic

Semiconductors: Aggregate Emission in Regioregular Polythiophene. *Phys. Rev. Lett.* **2007**, *98*, 206406.

(40) Cheng, H.-L.; Lin, J.-W.; Jang, M.-F.; Wu, F.-C.; Chou, W.-Y.; Chang, M.-H.; Chao, C.-H. Long-Term Operations of Polymeric Thin-Film Transistors: Electric-Field-Induced Intrachain Order and Charge Transport Enhancements of Conjugated Poly(3-hexylthiophene). *Macromolecules* **2009**, *42*, 8251−8259.

(41) Clark, J.; Chang, F. C.; Spano, F. C.; Friend, R. H.; Silva, C. Determining Exciton Bandwidth and Film Microstructure in Polythiophene Films Using Linear Absorption Spectroscopy. *Appl. Phys. Lett.* **2009**, *94*, 163306.

(42) Noriega, R.; Rivnay, J.; Vandewal, K.; Koch, F. P. V.; Stingelin, N.; Smith, P.; Toney, M. F.; Salleo, A. A General Relationship between Disorder, Aggregation and Charge Transport in Conjugated Polymers. *Nat. Mater.* **2013**, *12*, 1038−1044.

(43) Sirringhaus, H.; Brown, P. J.; Friend, R. H.; Nielsen, M. M.; Bechgaard, K.; Langeveld-Voss, B. M. W.; Spiering, A. J. H.; Janssen, R. A. J.; Meijer, E. W.; Herwig, P.; de Leeuw, D. M. Two-Dimensional Charge Transport in Self-Organized, High-Mobility Conjugated Polymers. *Nature* **1999**, *401*, 685−688.

(44) Credgington, D.; Durrant, J. R. Insights from Transient Optoelectronic Analyses on the Open-Circuit Voltage of Organic Solar Cells. *J. Phys. Chem. Lett.* **2012**, *3*, 1465−1478.

(45) Heumueller, T.; Mateker, W. R.; Sachs-Quintana, I. T.; Vandewal, K.; Bartelt, J. A.; Burke, T. M.; Ameri, T.; Brabec, C. J.; McGehee, M. D. Reducing Burn-in Voltage Loss in Polymer Solar Cells by Increasing the Polymer Crystallinity. *Energy Environ. Sci.* **2014**, *7*, 2974−2980.

(46) He, Y.; Chen, H.-Y.; Hou, J.; Li, Y. Indene−C60 Bisadduct: A New Acceptor for High-Performance Polymer Solar Cells. *J. Am. Chem. Soc.* **2010**, *132*, 1377−1382.

(47) Li, H.; Zhang, Z.-G.; Li, Y.; Wang, J. Tunable Open-Circuit Voltage in Ternary Organic Solar Cells. *Appl. Phys. Lett.* **2012**, *101*, 163302.

(48) Chang, M.; Choi, D.; Fu, B.; Reichmanis, E. Solvent Based Hydrogen Bonding: Impact on Poly(3-hexylthiophene) Nanoscale Morphology and Charge Transport Characteristics. *ACS Nano* **2013**, *7*, 5402−5413.